Role of Micellar Entanglement Density on Kinetics of Shear Banding Flow Formation: Experiments and a Comparison with the VCM model

Peter Rassolov,[1] Lin Zhou,[2] Pamela L. Cook,[3] and Hadi Mohammadigoushki[1, a)]

[1)] *Department of Chemical and Biomedical Engineering, FAMU-FSU College of Engineering, Tallahassee, FL 32310, USA.*

[2)] *Department of Mathematics, New York City College of Technology, Brooklyn, NY 11201, USA*

[3)] *Department of Mathematical Sciences, University of Delaware, Newark, DE 19716, USA*

(Dated: 14 January 2022)

We investigate the effects of micellar entanglement density on the kinetics of shear banding flow formation in a Taylor-Couette flow via a combination of experiments and simulations of the Vasquez-Cook-McKinley (VCM) model. In experiments, three sets of wormlike micellar solutions, each set with a similar fluid elasticity and zero-shear-rate viscosity, but with varying entanglement densities, are studied under start-up of steady shear. Our experiments indicate that in the set with the low fluid elasticity, the transient shear banding flow is characterized by the formation of a transient flow reversal in a range of entanglement densities. Outside of this range, the transient flow reversal is not observed. For the sets of medium and high elasticities, the transient flow reversals exist for relatively small entanglement densities, and disappear for large entanglement densities. Our analysis shows that wall slip and elastic instabilities do not affect this transient flow feature. Consistent with experiments, simulations of the VCM model predict that as the micellar entanglement density increases, the strength of the transient flow reversal first increases, then, at a higher entanglement density, the transient flow reversal weakens. We identify a correlation between micellar entanglement density, the width of the stress plateau, and the extent of the transient flow reversal. As the micellar entanglement density increases, the width of the stress plateau first increases, then, at a higher micellar entanglement density, plateau width decreases. Therefore, we hypothesize that the transient flow reversal is connected to the micellar entanglement density through the width of the stress plateau.

[a)] hadi.moham@eng.famu.fsu.edu

I. INTRODUCTION AND BACKGROUND

Surfactants and salts in aqueous solutions can self-assemble into micelles of different shapes, and among them are wormlike micelles (WLMs), which are long flexible cylindrical assemblies of surfactant molecules. WLMs that form entangled networks exhibit strong viscoelastic properties that make them useful in various practical applications such as in personal care products[1], oil-gas fields[2], and as model viscoelastic systems for fundamental research[3,4]. In particular, the viscoelastic properties of WLMs can be tuned as needed by adjusting the types and concentrations of the surfactants and salts.

One common and well-studied flow phenomenon observed in some WLMs is shear banding. Shear banding is associated with the formation of (at least) two co-existing bands of different shear rates that undergo the same shear stress[5,6]. Our understanding of the shear banding in WLMs is advanced in Taylor-Couette (TC) flows (flow between two concentric cylinders)[5,7,8]. A key aspect of the shear banding flows that has been studied is the kinetics of shear banding flow formation upon inception of flow; i.e., the temporal evolution of flows before a quasi-steady shear banded flow is established[9–17]. Recent studies in TC flows have shown that the kinetics of shear banding flow formation in WLMs feature wall slip[11,12,15,16,18–21], elastic instabilities[10,20,22,23], micellar alignment[24,25] and transient flow reversal[17,26]. In principle, the kinetics of the shear banding flow formation can be influenced by two factors; (i) the TC flow geometry and (ii) material properties of the WLMs. The effects of flow geometry, in particular the surface conditions of the flow cell, have been studied fairly extensively[15,27]. Lettinga and Manneville showed that modification of the surfaces of the TC cell affects the kinetics of shear banding flow formation through enabling or preventing wall slip. Wall slip can interfere with shear banding but can be diminished by roughening the surfaces in the measurement cell[15]. In transient flow, Mohammadigoushki and coworkers[17] quantified wall slip in start-up flow for a CTAB/NaSal solution using rheo-PTV and found that wall slip is most prominent at two times: (1) immediately after the start of applied shear, and (2) as the high shear band initially forms. Additional studies have illustrated that as the high shear band initially forms, the interface between the high and low shear bands becomes unstable due to formation of secondary flows in the high shear band near the inner rotating cylinder[27–30].

While the effects of TC flow geometry have been studied, less is known about the effects of material properties of WLMs on the kinetics of shear banding flow formation based on experiments. Our group has recently started investigating the role of material properties on the kinetics of shear banding flow formation in experiments. In particular, Mohammadigoushki and coworkers[17] observed a transient flow feature in flows of shear banding CTAB/NaSal WLMs. When a steady shear flow is first applied, there may be a temporary reversal in flow direction in part of the flow field during the formation of the steady-state shear-banding flow, which occurs during the transient stress decay period[17]. By comparing these observations with the predictions of the Vasquez-Cook-McKinley (VCM) model, the authors suggested that these transient flow reversals are associated with a relatively high fluid elasticity E[17] compared to prior literature reporting experiments of transient flow evolution of WLMs[14–16]. According to the predictions of the VCM model, the transient flow reversal occurs only beyond a critical fluid elasticity number, E ($E = \mathrm{Wi}/\mathrm{Re}$, where $\mathrm{Wi} = \lambda\dot{\gamma}$, $\mathrm{Re} = \rho\dot{\gamma}d^2/\eta_0$. Here, λ is the fluid relaxation time, $\dot{\gamma}$ is the shear rate, ρ is the fluid density, d is the gap size, and

η_0 is the zero-shear viscosity) and the dimensionless applied shear ramp-up rate a ($a = \lambda/t_s$ where t_s is the duration of the initial shear ramp)[31,32]. This conclusion was confirmed in a subsequent study by Rassolov and Mohammadigoushki[26], which reports a critical threshold in E and a beyond which a transient flow reversal is observed.

Besides the VCM model, predictions of transient flow reversals have been reported using the diffusive Rolie-Poly (DRP) model[33]. Adams et al. showed that the formation of transient flow reversals in viscoelastic polymer solutions depends on the polymer entanglement density, Z, and the viscosity ratio, $\beta = \eta_s/\eta_p$, where η_s is the solvent viscosity and $\eta_p \approx \eta_0 - \eta_s$ is the solute zero-shear viscosity. In our recent experimental study, we found that increasing the value of the micellar entanglement density Z at a constant fluid elasticity may tend towards transient flow reversal[26]; however, this observation is based on one comparison. A systematic study is needed to fully understand the effect of micellar entanglement density Z on the transient evolution of shear banding flows. Therefore, the main objective of this study is to assess the effect of Z on this flow feature using both experiments and simulations. In the following sections, we will present a systematic study of a start-up flow evolution for sets of WLMs where the value of Z is varied while those of the other relevant material parameters (particularly E and β) are held nearly fixed. We will report both experimental evidence of the effect of Z on transient flow evolution from rheo-optical measurements in a TC cell and a corresponding study of transient flow evolution predictions using the VCM model.

II. EXPERIMENTS

A. Materials

Fluids were prepared in the same manner as in our prior work[26]. Cetyltrimethylammonium bromide (CTAB) and sodium salicylate (NaSal) were mixed in deionized water. Both solutes were obtained from Millipore Sigma and used as received. Following mixing, solutions were kept sealed and away from ambient light for a minimum of two weeks prior to any measurements. For rheo-PTV experiments, glass microspheres (Potters 110P8, diameter $\approx 8\mu$m) were mixed at 50 ppm by mass along with the solutes. For visualization of flow instabilities, mica flakes (Jacquard PearlEx 671) were added at 250 ppm in a similar manner.

B. Fluid characterization

To find the relaxation time and the entanglement density of the fluids, linear viscoelastic data were measured using Small-Amplitude Oscillatory Shear (SAOS) experiments in an Anton-Paar MCR 302 with an off-the-shelf TC measuring cell with dimensions $R_i = 13.328$ mm, $R_0 = 14.449$ mm, and $h = 40$ mm. Here R_i and R_0 refer to inner and outer radii respectively, and h is the height of the TC cell. To assess the micellar entanglement density, the local minimum in the loss modulus (G'') where the elastic modulus (G') approaches

a plateau is needed (see details below). For several of the selected fluid preparations, the local minimum in the loss modulus occurs at a fairly high frequency, near 100 radians/s. This is close to the high frequency limit accessible in SAOS experiments beyond which measurements have significant errors due to inertia in the measuring system. For fluid preparations where the minimum in G'' is at or near this limit, a different method based on Diffusing Wave Spectroscopy (DWS) was used to extend the measured frequency spectrum to higher frequencies. For DWS experiments, fluids were prepared with 1% by mass of latex spheres (Life Technologies, $R = 300$ nm) and measured using a commercially available DWS instrument, LS Instruments RheoLab II, in 5 mm cuvettes with a 300 s multi-tau measurement time and a 60 s echo time. A preparation of 1% latex spheres in DI water was used to obtain the mean free path length l^* for DWS measurements.

To mfind the zero-shear viscosity and the high and low shear rate limits of shear banding, steady shear stress measurements were completed at shear rates from 0.001 to 100 s^{-1} in the same measurement cell as for SAOS. The viscosity was measured over time under each applied shear rate until it reached a steady value or quasi-steady oscillation, and either the steady value or the average value over several oscillations respectively was used to assemble the flow curve.

C. Rheo-optical measurements

Rheo-optical measurements were completed using a custom-built TC cell with $R_i = 13.35$ mm, $R_o = 14.53$ mm, and $h = 50$ mm. Details of the cell design and operation are given in our previous work[17,26]. Different from our previous work, the inner cylinder in this study was roughened by sandblasting in order to reduce wall slip. Several attempts to reduce wall slip at the outer cylinder were tested (discussed in detail in the following section). Additionally, all rheo-optical measurements were completed under initially applied steady shear rate flow with the shortest possible ramp-up duration (measured to be 0.1 s). Spatially and temporally resolved fluid velocity was measured using rheo-PTV. As in our previous work, the fluids were prepared with glass microspheres, and a laser (with wavelength of 532 nm) and a high speed camera (Phantom Miro 310) were used to image the flow plane. Particle trajectories were obtained from short clips of the video of the flow (much shorter than the time scales of flow evolution) using a Python script based on the TrackPy library[34] and (in the same script) averaged over small intervals along the radial axis to obtain spatially resolved velocity data with quantified uncertainty. In a modified version of the script, the above analysis was repeated for many consecutive intervals throughout longer videos to obtain a spatiotemporal map of either start-up or quasi-steady flow velocity.

In addition to rheo-PTV, flow instabilities were visualized using the fluids prepared with mica flakes, which orient to the flow direction and reflect light in an orientation-dependent manner. The fluid in the TC cell was illuminated by a desk lamp, and videos of the fluid under start-up of a shear flow were captured using a USB video camera (SenTech STC-MBS241U3V) aimed along the axis of the TC cell (i.e. imaging the $\theta - z$ plane). A Python script was used to assemble the video frames into a static image showing spatiotemporal evolution of the flow pattern. Further details of such visualizations are given in our previous work[35].

D. Modifications of the Taylor-Couette cell surfaces and the effect on wall slip

Shear banding systems under start-up of shear flow are known to exhibit wall slip during both the initial transient evolution and the quasi-steady state. Previous work with our apparatus has featured wall slip at both the inner and the outer cylinders of the TC cell[17,26]. The wall slip at the TC cell surfaces may affect the kinetics of shear banding flow formation[15]. Therefore, we have attempted to reduce the wall slip at both inner and outer cylinders by modifying the TC cell surfaces. The inner cylinder was roughened by sandblasting. Since the outer cylinder must remain optically transparent to allow for velocimetry and flow visualization, it cannot be roughened. Instead, it was modified in three different ways: (i) The outer cylinder was made hydrophobic by functionalizing with octyltrichlorosilane (i.e. silanized). (ii) A separate outer cylinder was cleaned by the RCA-1 protocol (5:1:1 water:ammonium hydroxide (25%):hydrogen peroxide(30%)) to obtain a hydrophilic surface. (iii) A third outer cylinder was coated with a screen protector (Vivitar VIV-SS-45) to increase the surface roughness and hydrophobicity slightly. Prior studies have shown reduction in wall slip when the screen protector was applied[36].

Fig. 1 shows the transient evolution of shear stress at the inner cylinder and the temporal evolution of velocity profiles in the Taylor-Couette cell for one of the selected fluid preparations (see Table I below) under start-up of steady shear flow with different surfaces. Although there is little difference in the evolution of shear stress with time for the different surfaces, the measured velocity profiles show significant differences. For untreated inner and outer cylinders, this solution exhibits a slight transient flow reversal right after the onset of stress decay and a significant wall-slip during quasi-steady flows. For a roughened inner cylinder, the quasi-steady wall-slip at the inner cylinder still exists, but the transient flow reversal becomes stronger than the experiments with the smooth inner cylinder. In Fig. 1 (d,e), the roughened inner cylinder is used with the functionalized outer cylinder and the screen protector on the outer cylinder respectively. For such conditions, the wall-slip at the outer cylinder is no longer negligible and the transient flow reversal is not observed for either of these surface treatments. Therefore, changing the surface of the outer cylinder (whether it is made hydrophilic or hydrophobic) not only leads to stronger wall-slip at the outer cylinder, but also changes the kinetics of shear banding flow formation by diminishing the transient flow reversal. To minimize wall slip and the resulting suppression of transient flow reversal, we completed the remainder of this work with a sandblasted inner cylinder and an untreated outer cylinder.

III. RESULTS AND DISCUSSIONS

A. Fluid Selection and Characterization

Following characterization of the linear and non-linear viscoelastic properties of the micellar solutions, three sets of fluid preparations, each with closely matched E, closely matched η_0, and broadly varied Z, were identified. Fig. 2 shows the rheological results for these samples, and the sample compositions and the rheological properties are listed in

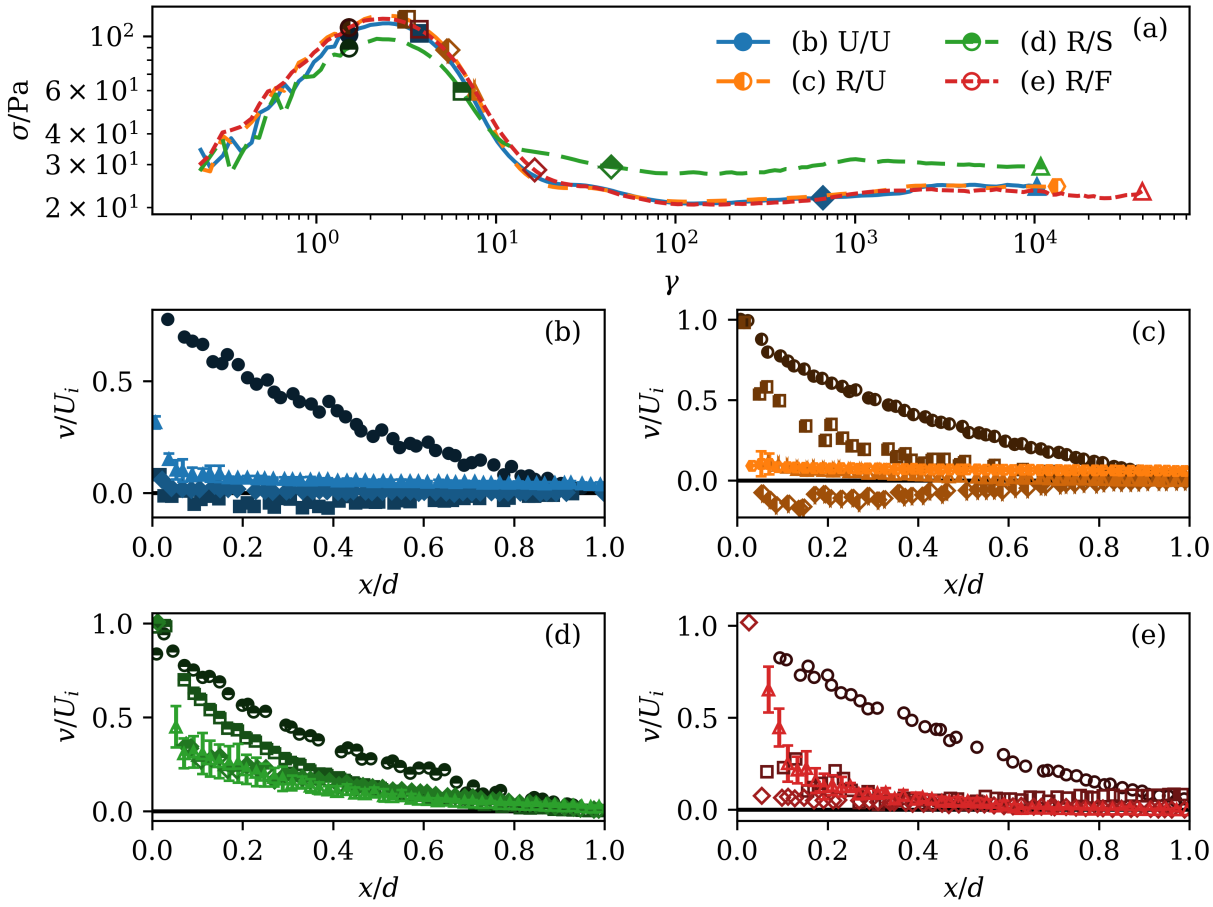

FIG. 1. Transient flow evolution for Wi = 20, $Z = 57$, $E = 1.56 \times 10^5$ with different surface treatments at the (inner/outer) cylinders: U, untreated; R, roughened; S, silanized; F, film applied (screen protector). (a) Shear stress evolution with shear strain. (b-e) Temporal evolution of normalized velocity profiles measured in the gap of the TC cell at selected shear strains. Symbols used in (b-e) correspond to those plotted on the shear stress curves in (a), and U_i is the applied velocity at the inner cylinder.

Table I. The micellar entanglement density, Z, cannot be measured directly in experiments. However, previous theoretical studies have provided approximate equations that can be used to assess Z in linear wormlike micellar solutions. Cates and Granek[37] developed a scaling relationship that links the micellar entanglement density to the measured storage and loss moduli in the fast breaking regime as $Z_{CG} \sim (G_0/G''_{min})$, where G_0 and G''_{min} respectively denote the plateau modulus and the local minimum in the loss modulus at high frequencies for which the storage modulus shows a plateau. Later, Granek[38] incorporated the effects of fluctuations in contour-length and suggested an improved version of this scaling relation as $Z_G^{0.82} \approx (G_0/G''_{min})$. More recently, Larson and co-workers used the simulations of their pointer algorithm and through fitting to experimental data for a series of micellar solutions, suggested the following scaling relationship[39]:

$$0.317\ Z^{0.82} \approx (G'_{min}/G''_{min}) \tag{1}$$

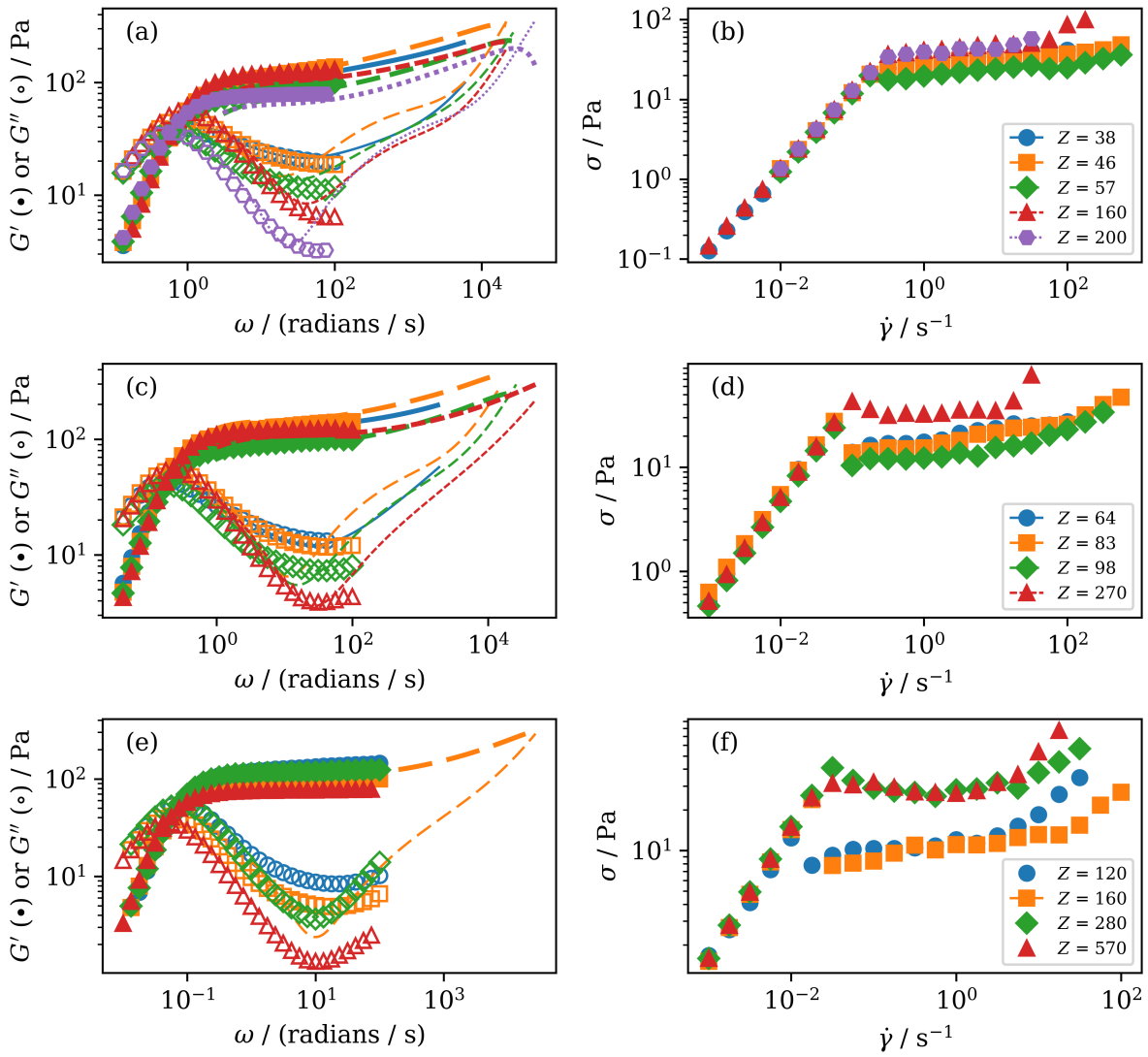

FIG. 2. Rheological properties for selected fluid conditions. (a,c,e) Frequency response data shown as SAOS storage modulus (filled symbols) and loss modulus (open symbols), and adjusted DWS storage modulus (thick curves) and loss modulus (narrow curves) low E (a), medium E (c) and high E (e) sets in Table I. (b,d,f) Flow curves for the same conditions as shown in (a,c,e) respectively.

where G'_{min} is G' at the same angular frequency as G''_{min}.

Eq. (1) differs from the scaling relation of Granek in that the prefactor of unity and the plateau modulus are replaced with a prefactor of 0.317 and the storage modulus at the frequency for which loss modulus shows a local minimum. In our study, we primarily use Larson's relation to estimate the micellar entanglement density; however, we also report the estimate according to Granek's relation. In order to do so, the rheological properties G'_{min} and G''_{min} are needed for the former, and G_0 and G''_{min} are needed for the latter. For our selected fluid preparations, G_0 can be measured from SAOS results obtained by mechanical rheometry. However, for some WLMs, G''_{min} and G'_{min} are not captured within the range of frequencies accessible by this method ($\omega \leq 100$ rad/s). To obtain higher frequency linear viscoelastic response of such fluids, we used DWS. DWS results were fitted

Fluid	CTAB/NaSal (mM/mM)	T(°C)	Z_{CG}	Z	η_0(Pa·s)	$E \times 10^5$
Low E	250/45	25	6.2	38	123	1.45
	250/50	28	7.4	46	130	1.38
	200/50	30	8.7	57	122	1.56
	200/70	38	20	160	136	1.17
	150/67.5	40	25	200	133	1.77
Medium E	250/45	19	9.6	64	533	23.9
	250/50	22	12	83	576	21.1
	200/50	25	14	98	472	20.0
	200/70	32	32	270	513	19.2
High E	250/50	17	16	120	1670	175
	200/50	20	20	160	1540	204
	200/70	27	32	280	1600	180
	150/67.5	29	57	570	1590	251

TABLE I. List of shear banding wormlike micellar solutions used in this study and the rheological characteristics. Z_{CG} is the estimate of the entanglement density according to the Cates and Granek scaling law, and Z is the estimate according to the Larson scaling relation.

to mechanical rheometry results by multiplying the storage and loss moduli by an optimized prefactor. This fitting procedure and its theoretical justification are described in detail by Larson and co-workers[40] and are plotted as the dashed lines in Fig. 2. The DWS method is only reliable for frequencies beyond 10 rad/s and is known to deviate from the mechanical rheology data for which G' is of much larger magnitude than G''[41]. Therefore, accurate and reliable DWS results could not be obtained for WLMs with high entanglement density, and hence, DWS results are not plotted for such fluid preparations. However, G'_{min} and G''_{min} for these particular fluid preparations can be estimated reliably from mechanical rheometry data alone.

B. Impact of the imposed Weissenberg number

As mentioned above, the main objective of this study is to assess the impact of micellar entanglement density on transient flow reversal, and wall slip may obscure the true impact of the micellar entanglement on this flow feature. The transient and quasi-steady wall slip both depend on the imposed Weissenberg number (Wi), as has been reported in the literature[15,18]. Therefore, before addressing the impact of micellar entanglement density, we assessed the impact of the applied Wi on the transient flow reversal in prepared fluids and identified the applied Wi that produced the maximum transient flow reversal (or equivalently the minimum wall slip). Fig. 3 shows the temporal evolution of the shear stress and velocity profiles for a selected fluid preparation at different applied Wi. Below the onset of shear banding, the transient flow reversal is not observed. For values of Wi that correspond to the onset of shear banding (Wi $\approx$ 2-5) the transient flow reversal is not observed due to significant wall slip at the outer cylinder. At high Wi numbers (50 and beyond) the transient flow reversal is very weak. Interestingly, at the intermediate values (Wi = 20), wall slip at

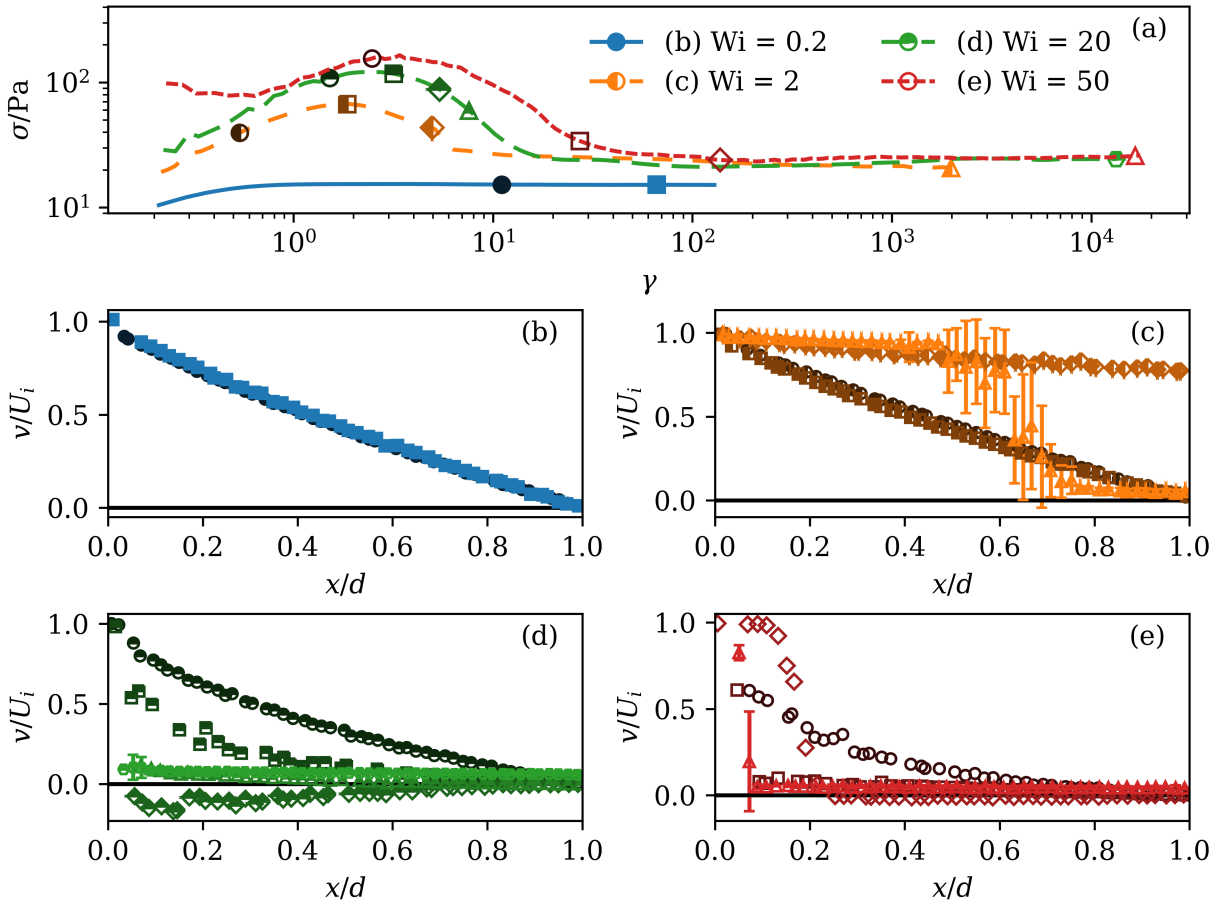

FIG. 3. Transient flow evolution for $Z = 57$, $E = 1.56 \times 10^5$ at different Wi. (a) Shear stress evolution with shear strain. (b-e) Temporal evolution of normalized velocity profiles measured in the gap of the TC cell at selected shear strains. Symbols used in (b-e) correspond to those plotted on the shear stress curves in (a), and U_i is the applied velocity at the inner cylinder.

the outer cylinder is minimal, and the transient flow reversal is at its maximum. This result was also confirmed for other fluid preparations (see Fig. S1 in the supplemental materials). Therefore, for the remainder of this work, we focus on the impact of micellar entanglement density at a fixed Weissenberg number Wi = 20 for which the transient flow reversal is at its maximum.

C. Effects of micellar entanglement density

Fig. (4) shows transient evolution of the flow for the set of micellar solutions with low E at Wi = 20 for various entanglement densities. For the lowest Z in this set, $Z = 38$, flow develops inhomogeneity (i.e., deviates from a linear velocity profile) during the stress overshoot, and this inhomogeneity then evolves to a shear banded profile. However, the elastic recoil is not strong enough to generate transient flow reversal. At longer times, a multiple-band quasi-steady velocity profile forms, which is characterized by two high shear bands

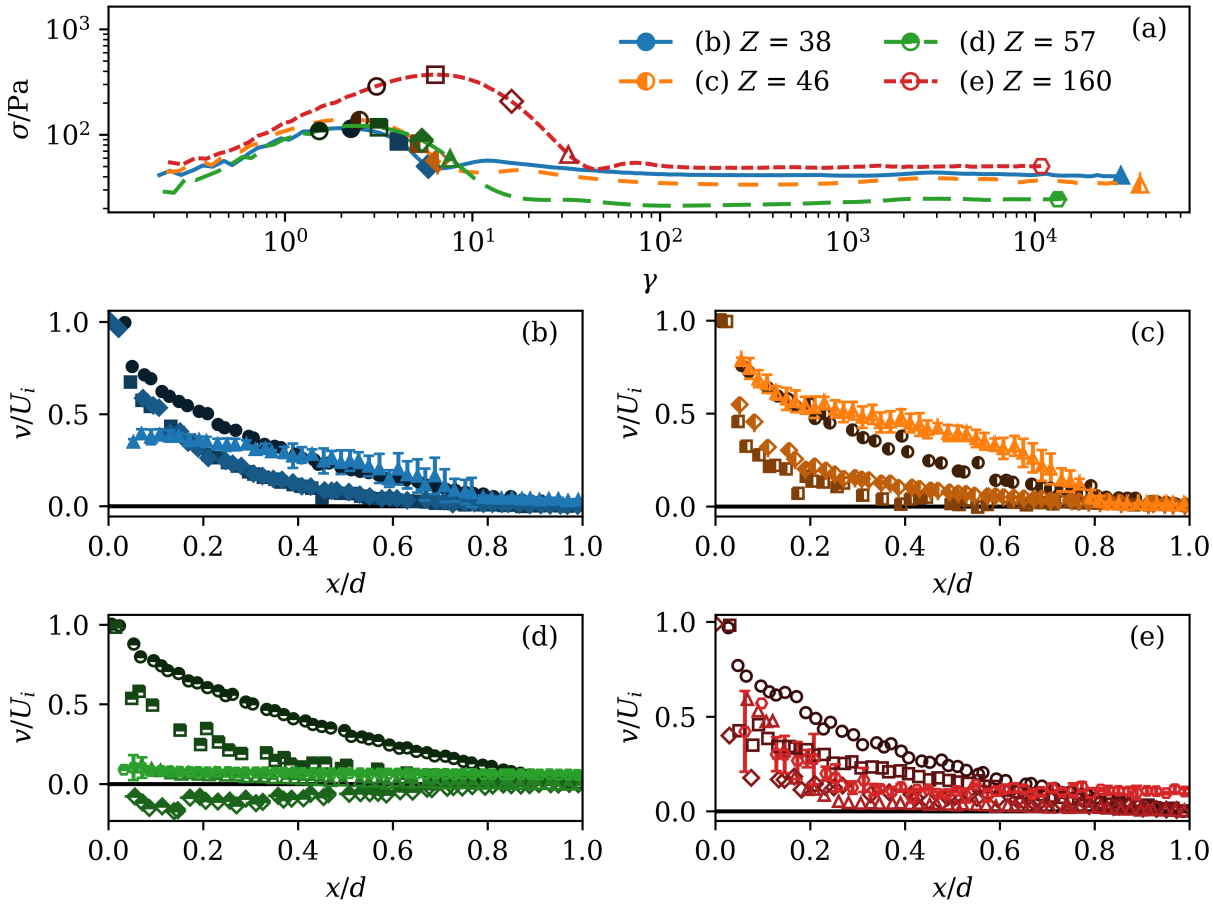

FIG. 4. Transient flow evolution for $E = (1.36 \pm 0.20) \times 10^5$ and Wi = 20 at varied Z. (a) Shear stress evolution with shear strain. (b-e) Temporal evolution of normalized velocity profiles measured in the gap of the TC cell at selected shear strains. Symbols used in (b-e) correspond to those plotted on the shear stress curves in (a), and U_i is the applied velocity at the inner cylinder.

and two low shear bands forming a high-low-high-low band order from the inner cylinder towards the outer cylinder. As Z increases slightly to 46, the flow inhomogeneity becomes more significant; however, the transient and quasi-steady flows are otherwise unchanged. At a still higher micellar entanglement density ($Z = 57$), the flow features a transient reversal in direction. A similar flow feature has been reported in prior literature for $E \sim 10^7$[17,26]; however, it had not been observed for such a low elasticity as $E = 1.56 \times 10^5$. Interestingly, as Z is increased to 160, the transient flow reversal disappears. Similar experiments were performed on the solutions with higher fluid elasticity. Fig. 5 shows the transient evolution of flow for the high E set. At the lowest micellar entanglement density from this fluid set ($Z = 120$), the flow features transient reversal followed by a quasi-steady two-banded flow. At higher entanglement densities ($Z = 160$), a similar behavior is reported. Beyond a critical micellar entanglement density (Z increased to 280), the transient flow reversal is no longer observed, and the quasi-steady flow features a sharp high shear band near the inner cylinder. A similar transition is reported for fluid sets with medium elasticity (see Fig. S2 in the supplementary materials).

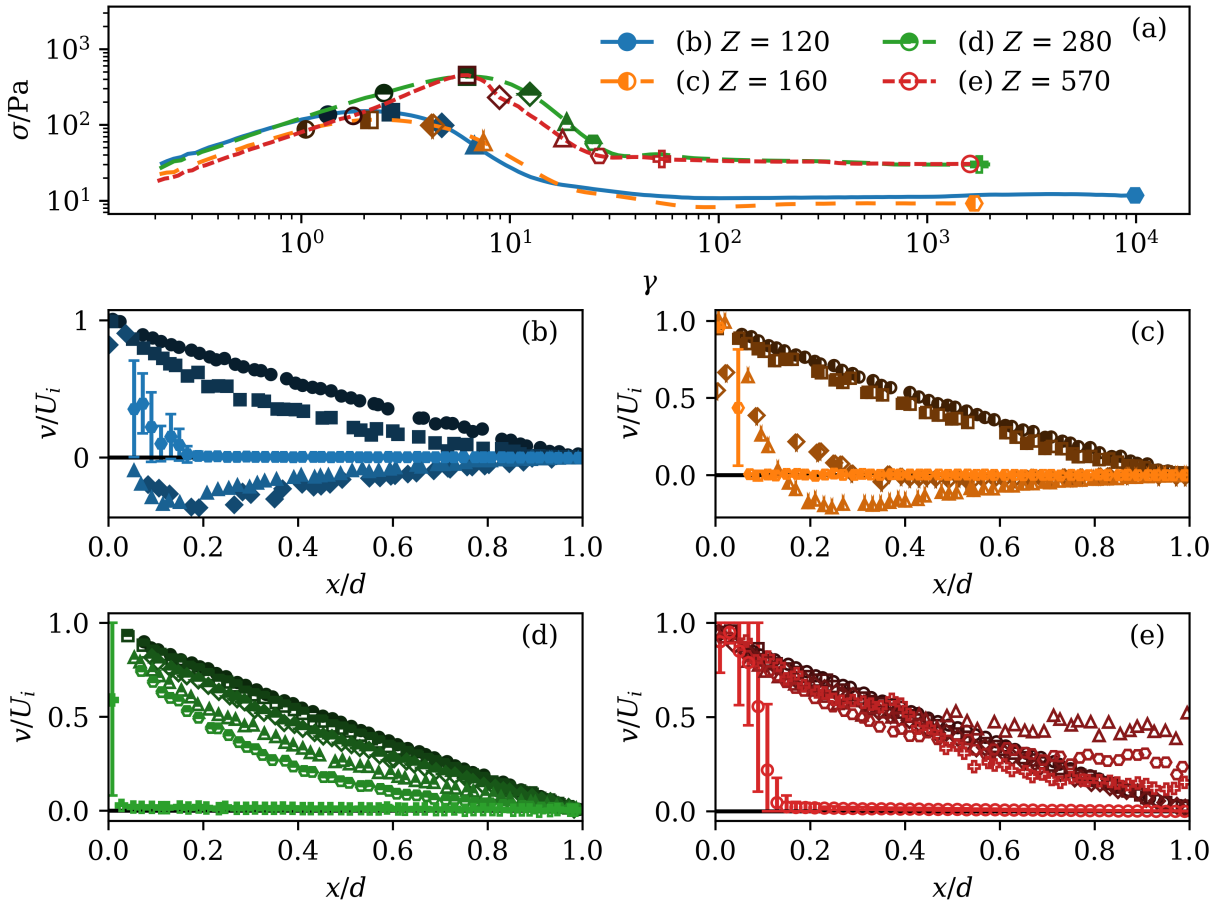

FIG. 5. Transient flow evolution for $E = (2.13 \pm 0.38) \times 10^7$ and Wi = 20 at varied Z. (a) Shear stress evolution with shear strain. (b-e) Temporal evolution of normalized velocity profiles measured in the gap of the TC cell at selected shear strains. Symbols used in (b-e) correspond to those plotted on the shear stress curves in (a), and U_i is the applied velocity at the inner cylinder.

Fig. (6) shows a summary of experimental results in terms of the transient and final quasi-steady flow response. For the fluids in the set with low elasticity, we observe two transitions in the kinetics of shear banding flow formation depending on the micellar entanglement density. The first transition is characterized by the appearance of transient flow reversal, while beyond a second critical threshold of micellar entanglement density, flow reversal is not observed. For fluids with higher elasticity, we only report the second transition. Moreover, Fig. 6(b) shows that the quasi-steady flow profile is characterized by multiple banded structures at the low fluid elasticity set and small micellar entanglement density. As the micellar entanglement increases beyond a critical threshold, the quasi-steady flow profile is characterized by a two-banded profile. At higher fluid elasticities, the quasi-steady flow forms a two-banded profile regardless of the micellar entanglement density.

The first transition observed in Fig. 6(a) is consistent with existing predictions of the DRP model[33]. According to the simulations of the DRP model, viscoelastic polymer solutions exhibit the transient flow reversal beyond a critical polymer entanglement density (see more detailed discussion below). However, to the best of our knowledge, the second

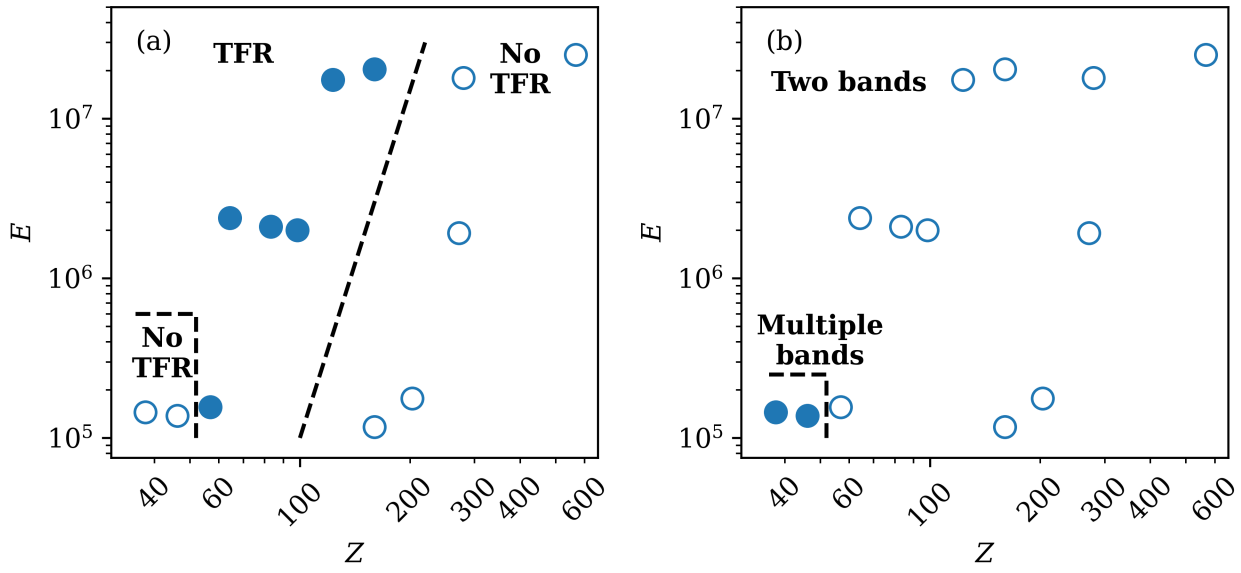

FIG. 6. A phase diagram summarizing the results of experiments. (a) Filled symbols indicate flow conditions that show transient flow reversals, while empty symbols indicate those that do not. (b) Filled symbols indicate flow conditions that lead to multiple-banded quasi-steady-state flow profiles, while empty symbols indicate those that are characterized by two-banded profiles.

transition observed in Fig. 6(a) is not reported in any model predictions.

D. Wall slip and flow instabilities

As noted in the above, flow of shear banding WLMs features wall slip as well as elastic instabilities. In this section, we will assess any possible connection between the second transition observed in Fig. 6(a) and the observed wall slip and/or elastic instabilities.

First, we assess the connection between transient flow reversals and wall slip. Fig. 7 shows the transient shear stress as a function of strain (a) along with transient wall slip at the inner and outer cylinders (b) for start-up shear flow at Wi = 20 for two of the fluid preparations from the low elasticity set and two from the high elasticity set. Spatiotemporal maps of the transient, local fluid velocity are presented in Fig.7 (c-f) for each of these four cases to provide a more complete visualization of the transient and quasi-steady flows. For the fluids from the set with the low elasticity, the flow evolution features transient flow reversal at the lower entanglement density $Z = 57$ (shown in Fig. 7(c)), while at the higher entanglement density $Z = 160$, no transient flow reversal is observed (shown in Fig. 7(d)). However, for both of them, the wall slip at the inner cylinder follows a similar trend during the initial transient evolution. Specifically, the wall-slip initially increases at the inner cylinder following the shear stress overshoot. Beyond a critical shear strain, a high shear band emerges near the inner cylinder, and this reduces the wall slip at the inner cylinder. Finally, in quasi-steady flow, the wall slip both at the inner and outer cylinders reemerges. Because the wall slip evolves similarly for both of these solutions during the initial transients, the lack of transient flow reversal at higher micellar entanglement density is not related to

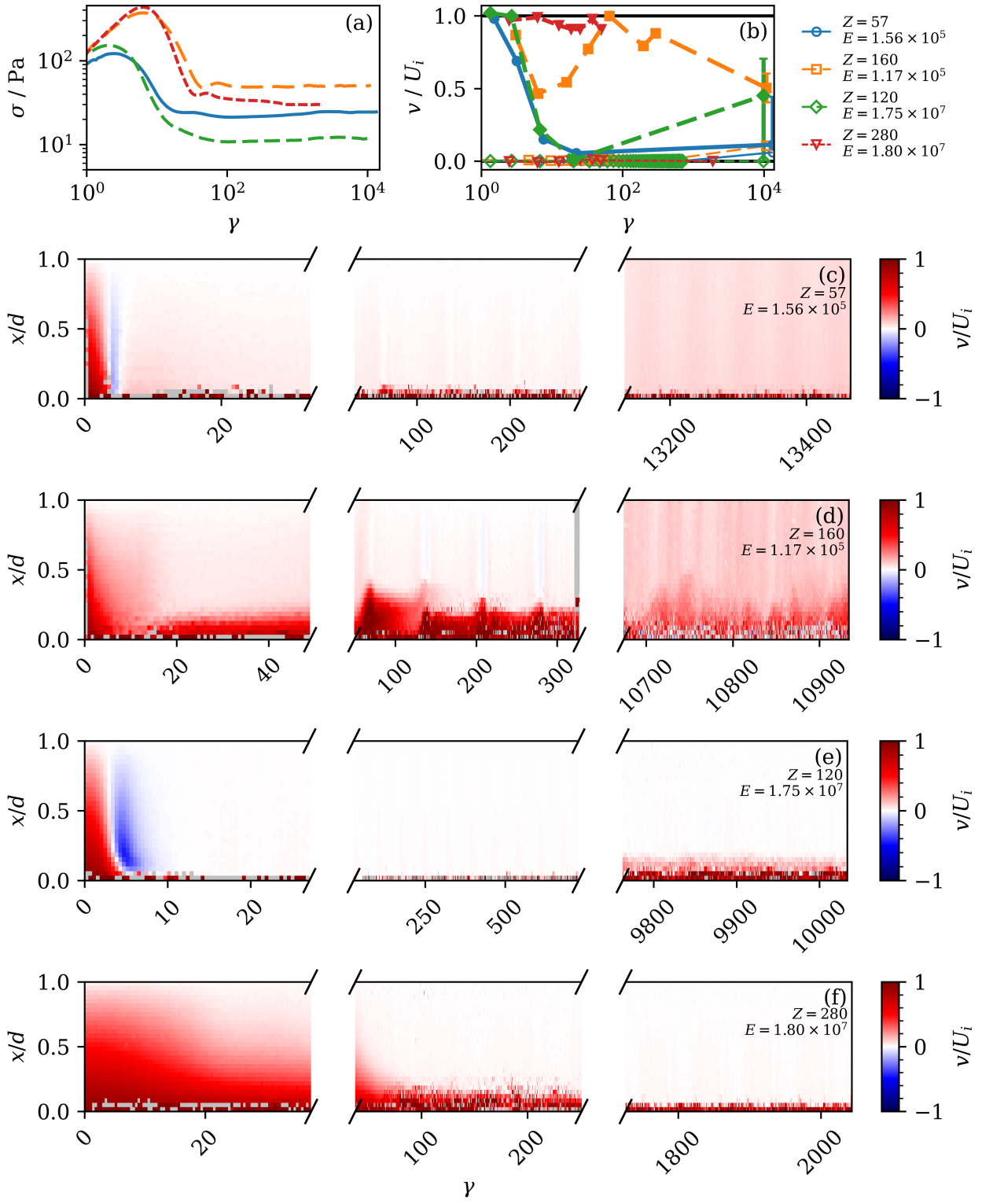

FIG. 7. Summary of transient wall slip and flow evolution for selected fluid preparations. (a) Shear stress evolution with shear strain. (b) Transient wall slip evolution with shear strain at the inner cylinder (filled markers) and the outer cylinder (empty markers). For $Z = 280$, optical distortions near the inner cylinder emerge around $\gamma = 50$, and quantification of wall slip at the inner cylinder is impossible. (c-f) Velocity maps for selected fluid preparations. (c) $Z = 57$, $E = 1.56 \times 10^5$. (d) $Z = 160$, $E = 1.17 \times 10^5$. (e) $Z = 120$, $E = 1.57 \times 10^7$. (f) $Z = 280$, $E = 1.80 \times 10^7$.

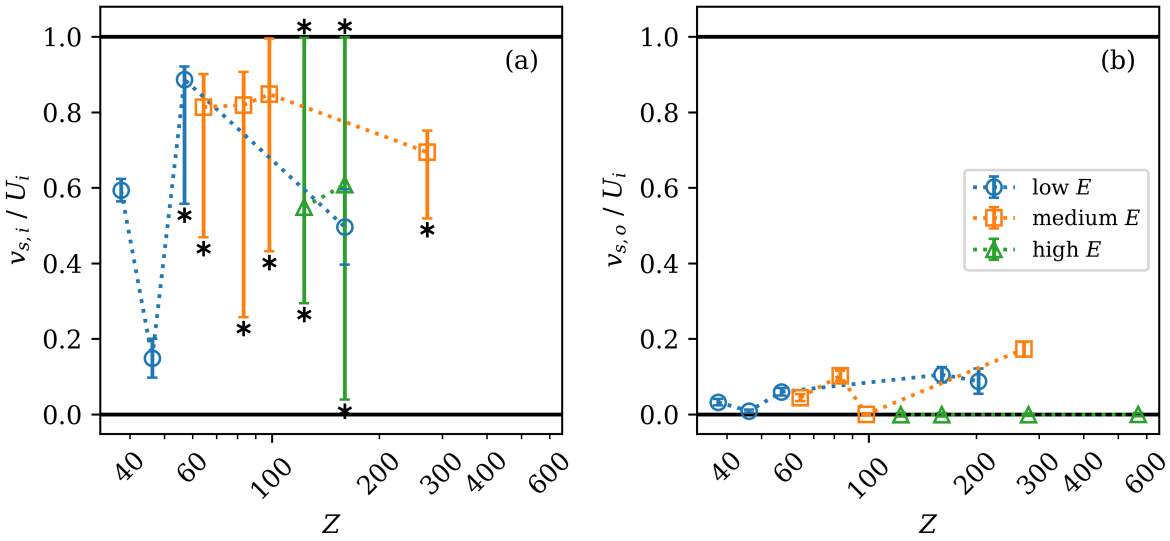

FIG. 8. Quasi-steady wall slip for each selected fluid preparation at the inner (a) and outer (b) cylinders, grouped by fluid elasticity E. Error bars marked with $*$ indicate the maximum observed extent of slip velocity deviation from the mean, while those without error bars indicate the standard deviation associated with the slip velocity, not exceeding relative slip velocities of 0 or 1.

the wall slip. A similar trend is observed for the fluids with high elasticities.

We also monitored the quasi-steady wall slip as a function of entanglement density for all selected fluid preparations. Fig. 8 shows the quasi-steady wall slip at the inner and outer cylinders as a function of micellar entanglement density. At the inner cylinder, the quasi-steady wall slip changes in a non-monotonic fashion as the entanglement density and fluid elasticity are increased. The wall slip measurements have high uncertainty due to temporal fluctuations in the quasi-steady velocity profiles. However, at the outer cylinder, entanglement density and elasticity affect the observed quasi-steady wall slip. For fluids with the low and medium elasticity sets, the quasi-steady wall slip at the outer cylinder is negligible at low entanglement density and increases as the entanglement density increases. However, for the fluids with high elasticity, the quasi-steady wall slip at the outer cylinder is negligible for the entire range of micellar entanglement densities.

Our earlier work[26] suggested that transient flow reversals in these solutions may be related to elastic instabilities that are known to arise in the flow of some shear banding WLMs[35]. Fig. 9 shows the evolution of the flow stability in the same fluids as shown in Fig. 8 subject to the same start-up steady shear flow. These fluids are prepared with mica flakes as described previously to reveal any secondary flows or other instabilities that may occur, which appear as variations in the imaged light intensity in the vorticity direction (x_3). For these fluids, visible indications of instabilities arise at around $\gamma \approx 500$ to 2000, which is well beyond the time scale where transient flow reversals are observed. This applies to all fluids reported in this paper. The transient flow reversal occurs just beyond the stress overshoot and around $\gamma \approx 5$. Therefore, as discussed in our earlier work, it is unlikely that the onset of flow instabilities is related to the occurrence of transient flow reversals.

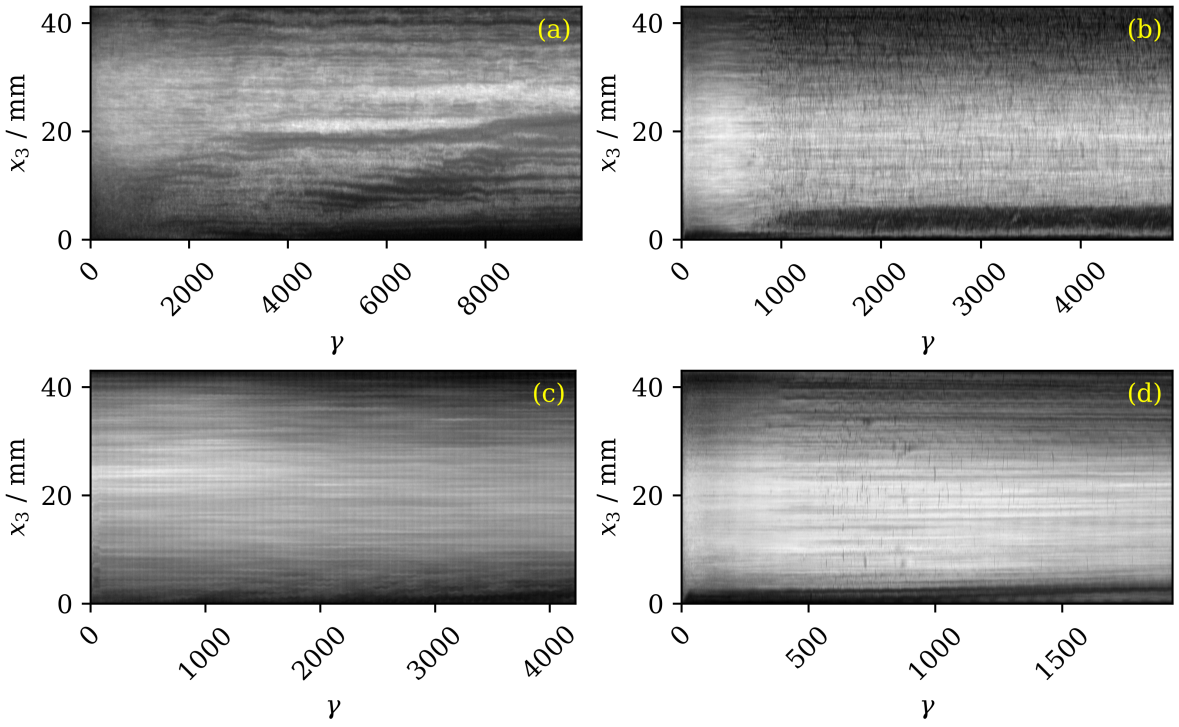

FIG. 9. Spatio-temporal evolution of the flow of WLMs subject to start-up of steady shear flow visualized using mica flakes for selected fluid preparations: (a) $Z = 57$, $E = 1.56 \times 10^5$. (b) $Z = 160$, $E = 1.17 \times 10^5$. (c) $Z = 120$, $E = 1.57 \times 10^7$. (d) $Z = 280$, $E = 1.80 \times 10^7$. Here, x_3 denotes the position along the TC cell axis.

E. Modeling

In order to better understand the effects of micellar entanglement density on the kinetics of shear banding flow formation, we performed time-resolved simulations of the VCM model. The VCM model is a two-species breaking/reforming model that has been used in prior published literature to study flows of WLMs[31,32,42]. Note that although the VCM model captures some important physics of the flow of WLMs such as micellar breakage and reformation, this model does not directly incorporate the effects of micellar entanglements in its constitutive equations. However, it does predict the formation of a plateau in the storage modulus and a minimum in loss modulus at high frequencies, the quantities that we have used to estimate the micellar entanglement density in our experiments.

The VCM model consists of nonlinear differential equations for the number densities (n_A, n_B) and the stress tensors ($\mathbf{A}, \mathbf{B}$) of each species A and B, respectively. The dimensionless

equations are:

$$\mu\frac{Dn_A}{Dt} = 2\delta_A\nabla^2 n_A - \delta_A\nabla\nabla : \mathbf{A} + \frac{1}{2}c_B n_B^2 - c_A n_A \tag{2a}$$

$$\mu\frac{Dn_B}{Dt} = 2\delta_B\nabla^2 n_B - \delta_B\nabla\nabla : \mathbf{B} - c_B n_B^2 + 2c_A n_A \tag{2b}$$

$$\mu\mathbf{A}_{(1)} + \mathbf{A} - n_A\mathbf{I} - \delta_A\nabla^2\mathbf{A} = c_B n_B\mathbf{B} - c_A\mathbf{A} \tag{2c}$$

$$\epsilon\mu\mathbf{B}_{(1)} + \mathbf{B} - \frac{n_B}{2}\mathbf{I} - \epsilon\delta_B\nabla^2\mathbf{B} = -2\epsilon c_B n_B\mathbf{B} + 2\epsilon c_A\mathbf{A}. \tag{2d}$$

The dimensionless breakage rate is $c_A = c_{A,eq} + (\mu\xi/3)(\dot{\gamma} : \mathbf{A}/n_A)$, and the dimensionless reforming rate is $c_B = c_{B,eq}$ in which $c_{A,eq}$ and $c_{B,eq}$ are the breakage and reforming rates at equilibrium. Further details of the model nondimensionalization, the model parameters, and the definitions of the notations can be found in prior literature[17,32]. To simulate inhomogeneous flow, the above constitutive equations are combined with the following conservation of momentum equation to yield the solutions of number densities, stresses and velocity profiles:

$$E^{-1}\frac{\partial\mathbf{v}}{\partial t} = -\nabla\cdot(P\mathbf{I} - \beta\dot{\boldsymbol{\gamma}} + \boldsymbol{\tau}_p). \tag{3}$$

In the momentum equation, the elasticity number is defined as $E = \lambda_{eff}\eta_0/\rho d^2$, in which λ_{eff} is the effective relaxation time of the mixture and corresponds to λ in experimental measurements. No-flux boundary conditions are used for the number densities and stresses. To obtain the linear viscoelastic model predictions, the model equations are linearized, and the storage and loss moduli reduce to a two-mode Maxwell model plus a viscous solvent:

$$G' = G_0\left\{\frac{(\lambda_{eff}\omega)^2}{1+(\lambda_{eff}\omega)^2} + n_B^0\frac{(\lambda_B\omega)^2}{1+(\lambda_B\omega)^2}\right\} \tag{4a}$$

$$G'' = G_0\left\{\frac{\lambda_{eff}\omega}{1+(\lambda_{eff}\omega)^2} + n_B^0\frac{\lambda_B\omega}{1+(\lambda_B\omega)^2}\right\} + \eta_s\omega. \tag{4b}$$

The first mode is determined by the system relaxation time. The second mode is determined by the B species, in which n_B^0 and λ_B are the dimensionless equilibrium number density and relaxation time of the B species, respectively.

The VCM model parameters are obtained by fitting model predictions to both the experimental SAOS data and the flow curve as follows. First, we use the SAOS data to fit the linear viscoelastic VCM model predictions. Using Equations (4a) and (4b), the system relaxation time (λ_{eff}) is obtained by identifying the maximum of the loss modulus G'' at low frequencies and its cross-over with G'. The minimum of G'' is related to the product $n_B^0\lambda_B$[42]. Increasing $n_B^0\lambda_B$ at fixed G_0 and λ_{eff} has two simultaneous and inseparable effects: the local minimum value of G'' increases, and the value of ω associated with this minimum decreases (an example of such dependence is shown in Fig. S3 in the supplementary materials). Fig. 10(a) shows the results of SAOS data fitting for the five cases in the low E group, and Fig. 10(c) shows the results for the medium E group. At high experimentally determined entanglement densities, the VCM model predictions are in good agreement with experimental data throughout the frequency range. However, at lower Z values, the mismatch between the experimental data and the simulation results is more pronounced; in

particular, the local minimum in the VCM loss modulus occurs at a much lower frequency than that in the experimental loss modulus. As noted above, the linearized VCM model consists of two Maxwell modes as reflected in the G' and G'' formulas, and the product $n_B^0\lambda_B$ simultaneously affects both the value of G'' at the local minimum and that of ω where it occurs. Since the purpose of these simulations is to produce a similar Z to those estimated for WLMs in experiments, we selected a value of the product $n_B^0\lambda_B$ that produces the same value of G''_{min} as that of the experiment, which will usually result in an unavoidable mismatch at the value of ω where this occurs.

The flow curves are used to fit the remaining parameters: n_B^0 and λ_B as resolved from one another, $\mu = \lambda_A/\lambda_{eff}$ (ratio of the relaxation times of the long species A and the effective relaxation time), and the partially extending strand parameter ξ which appears in the breakage rate c_A. From the homogeneous shear flow analysis[42], the shear stress at high shear rates is approximated by the relationship:

$$\tau_{p,r\theta} \sim \frac{2\lambda_B + n_B^0\lambda_B}{\lambda_{eff}}\dot{\gamma} = \frac{(2+n_B^0)\lambda_B}{\lambda_{eff}}\dot{\gamma}. \tag{5}$$

Fitting the flow curve at high shear rates informs the value of λ_B (Note, $n_B^0\lambda_B$ is already determined from SAOS data; however, n_B^0 and λ_B individually are not yet known.). The values of ξ and μ are determined by the position of the plateau and by modeling constraints. Knowing λ_B, $\mu = \lambda_A/\lambda_{eff}$, and ξ allows us to compute the remaining VCM parameters[42]. Fig. 10 (b,d) show the steady shear predictions of the VCM model along with flow curves obtained in experiments. For low shear rates, the VCM model predicted flow curves agree with the experimental data. At high shear rates, only the flow curves for the high Z fluid preparations agree with the VCM flow curves. For lower Z, the VCM flow curves predict the end of the stress plateau at lower shear rates than were measured in experiments. Using the above parameter space, we can compute the transient evolution of shear flows within the shear banding plateau for these cases.

Fig. 11 (a,b) show the VCM predicted maximum magnitude of the transient negative velocities within the gap of the Taylor-Couette cell as a function of imposed shear rate for each Z value in (a) the low E set and (b) the medium E set. Fig. S4 in the supplementary materials shows the process of obtaining this maximum negative velocity for each imposed Weissenberg number. At low fluid elasticity, increasing Z in the range from 38 to 160 leads to stronger transient flow reversal across a wide range of imposed Weissenberg numbers. However, beyond a critical threshold of $Z > 160$, the flow reversal becomes smaller. For $Z = 200$, the magnitude of the maximum negative velocity during the flow reversal is smallest. Although the VCM simulations show the transient flow reversal for all five preparations, these trends in the strength of the flow reversal are consistent with the experimental results. A similar behavior is predicted for medium elasticity fluids with respect to the micellar entanglement density (see Fig. 11 (b)). Note that at high fluid elasticity, the simulations of VCM model are currently not tractable and therefore are not discussed.

In summary, both experiments and simulations revealed a non-monotonic trend in the strength of the transient flow reversal with respect to the micellar entanglement density. As the micelles become more entangled, the strength of the transient flow reversal increases, but beyond a critical threshold of micellar entanglement density, the flow reversal weakens. Interestingly, there exists a correlation between the micellar entanglement density, the width

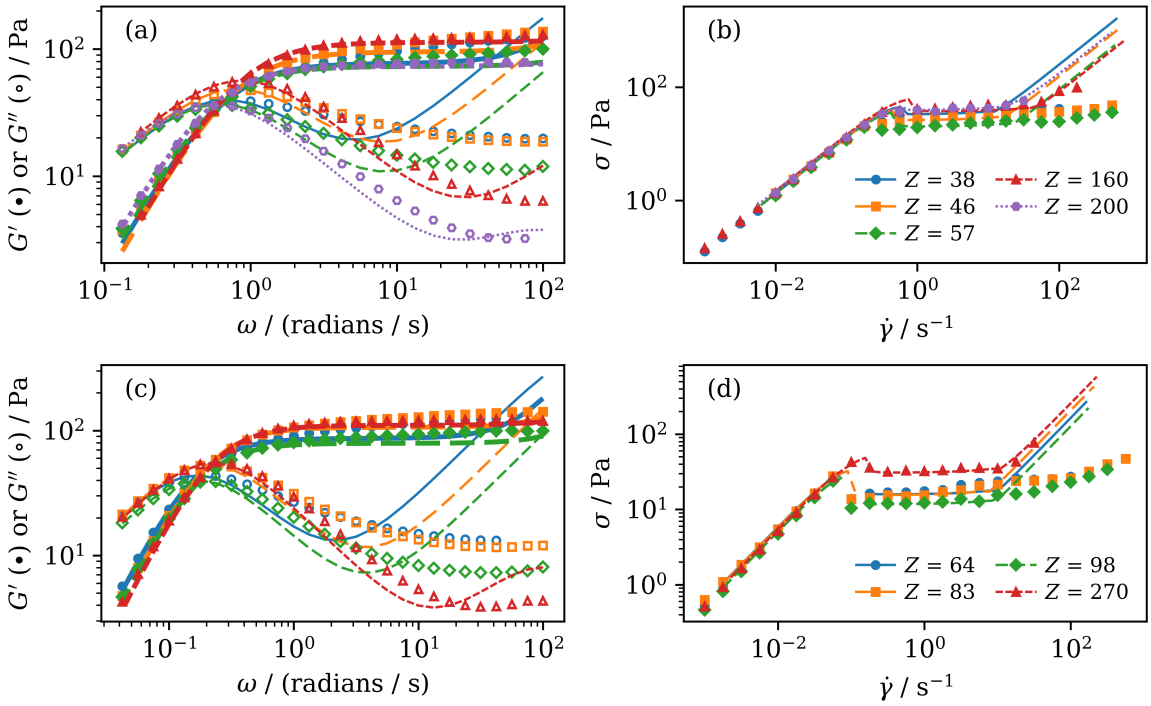

FIG. 10. Rheometry data and fitted VCM model predictions for (a,b) the low E set of fluid preparations and (c,d) the medium E set. (a,c) Experimentally obtained SAOS data (symbols) and linear viscoelastic predictions of the VCM model (lines). (b,d) Experimentally measured flow curves (symbols) and VCM model predicted flow curves for steady-state nonuniform flow (lines).

of the stress plateau, and the strength of the transient flow reversal both in experiments and simulations of the VCM model. Fig. 11(c) shows the greatest extent of the transient negative velocity as a function of the width of the stress plateau for both VCM simulations and experiments. As the width of the stress plateau increases, the transient flow reversal becomes stronger both in experiments and simulations.

The connection between the transient flow response and the width of the stress plateau can be rationalized as follows. Previous studies on shear banding WLMs[27,30] have shown that upon imposition of the startup shear flow within the shear banding regime, the flow inside the gap of the TC cell undergoes a series of transitions. First, a linear velocity profile develops across the gap. Then, a high shear band forms near the rotating inner cylinder. A kink in the velocity profile forms at the juncture of the high and low shear rate bands. In time the velocity at the kink may overshoot to negative velocity values (see Figs. 4(d) and 5(b,c)) before settling to the steady state value. This overshoot behavior is known as elastic recoil. Systems with a wider stress plateau shear band with a larger shear rate, slope in the velocity, close to the inner cylinder (see a schematic shown in Fig. S5 of the supplementary materials). As the slope of the velocity near the inner cylinder increases, the likelihood of a strong elastic recoil, thus the velocity reaching negative values during transient flow evolution, also increases.

Further investigation of the VCM model simulations shows a correlation between the

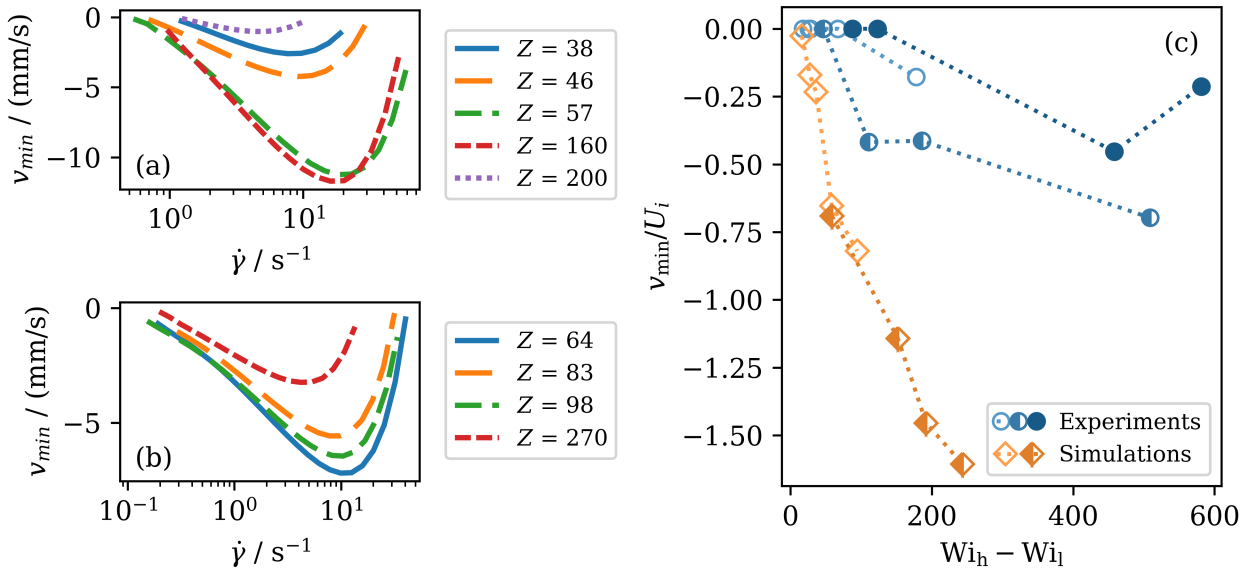

FIG. 11. (a,b) Fastest transient negative fluid velocities in start-up flow predicted by the VCM model for the parameter sets corresponding to (a) the low E set of fluid preparations; (b) the medium E set, over the ranges of shear rates where flow reversals are observed. (c) Maximum negative fluid velocities for Wi = 20 observed in experiments (blue circles) and predicted by the VCM model (orange diamonds), plotted as a function of stress plateau width for (lightest, empty symbols) the low E set of fluid preparations, (medium-tone, half-filled symbols) the medium E set, and (darkest, filled symbols, reported for experiments only) the high E set.

width of the stress plateau and the entanglement density Z. In the VCM model, the stress plateau width can be related to model parameters by rearranging Eq. (5) to obtain an expression for the slope of the flow curve in the high shear rate limit as:

$$\tau_{p,r\theta}/\dot{\gamma}_h \sim \frac{2\lambda_B + n_B^0\lambda_B}{\lambda_{eff}} = (2 + n_B^0)\frac{\lambda_B}{\lambda_{eff}} = \frac{2n_A^{0\prime} + n_B^{0\prime}}{n_A^{0\prime}}\frac{\lambda_B}{\lambda_{eff}} \tag{6}$$

in which the prime terms are dimensional number densities of A and B species in equilibrium, respectively. The high shear rate limit of the shear banding plateau ($\dot{\gamma}_h$) and correspondingly the width of the stress plateau are related to the inverse of $(2 + n_B^0)\lambda_B/\lambda_{eff}$. Using this simple scaling analysis, two regimes for the effect of n_B^0 on the stress plateau are expected. For $n_B^0 \ll 2$ (which refers to a system containing many A species but very few B species in equilibrium), $\tau_{p,r\theta}/\dot{\gamma}_h$ is dominated by the term $2\lambda_B/\lambda_{eff}$, therefore the width of the stress plateau is mainly controlled by $2\lambda_B$ term. Conversely, for $n_B^0 \gg 2$ (which refers to a system containing few A species but many B species in equilibrium), $\tau_{p,r\theta}/\dot{\gamma}_h$ is dominated by the term $n_B^0\lambda_B/\lambda_{eff}$, and the width of the stress plateau is mainly controlled by the value of $n_B^0\lambda_B$. To assess the above scaling analysis, we have provided a summary of the VCM parameters for the two fluid sets and various micellar entanglement densities in Table II. For the low E set and $Z = 38, 46, 57$, the width of the plateau is determined by $n_B^0\lambda_B$, and as Z increases, $n_B^0\lambda_B$ decreases so the plateau width increases. This trend continues until at even higher Z values when the dominant term switches to $2\lambda_B$. Increasing Z in this range, from 160 to 200, leads to an increase in $2\lambda_B$ thus a decrease in the stress plateau. Therefore in the low elasticity set, as Z increases from 38 to 200, the width of the plateau first increases then

decreases, and this non monotonic trend is consistent with the magnitude of the transient flow reversal observed in the experiment.

As mentioned in the introduction, the DRP model predicted the correlation between the transient flow reversal and the entanglement density[33]. The simulations of the transient flow of the DRP model also suggest that a stronger transient flow reversal is expected for wider stress plateaus as those of the VCM model, however, unlike the prediction of the VCM model, as the micellar entanglement density Z increases, the DRP model shows that the width of the plateau keeps widening monotonically which is different from the observation of the experimental data.

Z	$n_B^0\lambda_B$	$2\lambda_B$	$\tau_{p,r\theta}/\dot{\gamma}$
		Low E	
38	2.4×10^{-2}	4.8×10^{-3}	2.8×10^{-2}
46	1.2×10^{-2}	2.4×10^{-3}	1.4×10^{-2}
57	9.1×10^{-3}	1.8×10^{-3}	1.1×10^{-2}
160	1.0×10^{-3}	5.2×10^{-3}	6.2×10^{-3}
200	8.8×10^{-4}	2.0×10^{-2}	2.0×10^{-2}
		Medium E	
64	3.5×10^{-2}	7.0×10^{-3}	4.2×10^{-2}
83	1.4×10^{-2}	2.9×10^{-3}	1.7×10^{-2}
98	1.2×10^{-2}	2.4×10^{-3}	1.4×10^{-2}
270	1.4×10^{-3}	1.9×10^{-2}	2.1×10^{-2}

TABLE II. VCM model parameter expressions $n_B^0\lambda_B$ and $2\lambda_B$ associated with the shear stress plateau width, and the slope of the flow curve in the high shear rate limit predicted by Equation 5.

IV. CONCLUSIONS

In summary, we have studied the impact of the micellar entanglement density on the kinetics of shear banding flow formation in a range of shear banding wormlike micellar solutions both through experiments and through corresponding simulations of the VCM model. Our experiments show two critical transitions. First, as entanglement density increases for a fluid set with a fixed elasticity number, we observe the emergence of a transient flow reversal during the shear stress decay. This is consistent with our prior observations[26] and with DRP model predictions reported in the prior literature[33]. Surprisingly, beyond a second critical transition, the flow ceases to exhibit this transient flow reversal. The corresponding VCM simulations show a weak flow reversal for the lowest entanglement number that initially strengthens as the entanglement number is increased. The extent of flow reversal then goes through a maximum, beyond which it decreases with continued increase in the entanglement number. Therefore, the observed extent of transient flow reversal in shear banding flow formation depends on the entanglement density in a nontrivial manner.

To better understand the connection between the fluid entanglement density and the transient flow evolution, we compared extent of the flow reversal in experiments and in

simulations with the width of the shear stress plateau and identified a correlation: the extent of the transient flow reversal increases as the width of the stress plateau increases. However, the nature of connection between the micellar entanglement density and the width of the stress plateau remains to be understood.

V. ACKNOWLEDGEMENTS

We are grateful to Joseph Schlenoff (FSU Chemistry and Biochemistry) and Daniel Hallinan (FAMU-FSU College of Engineering) who have given us access to their labs for silanization of the Taylor-Couette cell. Diffusing wave spectroscopy experiments were performed using the LS RheoLab II instrument available in the Ramakrishnan lab (FAMU-FSU College of Engineering) that is supported by NSF CREST 1735968. This work is funded by NSF CBET CAREER 1942150. We are grateful to Peter Olmsted, Gareth McKinley and Geoffrey Reynolds for many helpful discussions.

REFERENCES

[1]Z. Chu, C. A. Dreiss, and Y. Feng, "Smart wormlike micelles," Chem. Soc. Rev. **42**, 7174–7203 (2013).
[2]R. Zana and E. E. Kaler, Giant Micelles: Properties and Applications (1st ed.). (CRC Press, 2007).
[3]M. E. Cates and S. M. Fielding, "Rheology of giant micelles," Advances in Physics **55**, 799–879 (2006), arXiv:0702047 [cond-mat].
[4]J. P. Rothstein and H. Mohammadigoushki, "Complex flows of viscoelastic wormlike micelle solutions," Journal of Non-Newtonian Fluid Mechanics **285**, 104382 (2020).
[5]T. Divoux, M. A. Fardin, S. Manneville, and S. Lerouge, "Shear Banding of Complex Fluids," Annual Review of Fluid Mechanics , 81–103 (2016), arXiv:1503.04130.
[6]N. A. Spenley, X. F. Yuan, and M. E. Cates, "Nonmonotonic constitutive laws and the formation of shear-banded flows," Journal de Physique II **6**, 551–571 (1996).
[7]S. Manneville, "Recent experimental probes of shear banding," Rheologica Acta **47**, 301–318 (2008), arXiv:0903.5389.
[8]P. D. Olmsted, "Perspectives on shear banding in complex fluids," Rheologica Acta **47**, 283–300 (2008).
[9]R. N. Al-kaby, J. S. Jayaratne, T. I. Brox, S. L. Codd, J. D. Seymour, and J. R. Brown, "Rheo-NMR of transient and steady state shear banding under shear startup," Journal of Rheology **62**, 1125–1134 (2018).
[10]R. N. Al-kaby, S. L. Codd, J. D. Seymour, and J. R. Brown, "Characterization of velocity fluctuations and the transition from transient to steady state shear banding with and without pre-shear in a wormlike micelle solution under shear startup by Rheo-NMR," Applied Rheology **30**, 1–13 (2020).
[11]L. Bécu, S. Manneville, and A. Colin, "Spatiotemporal dynamics of wormlike micelles under shear," Physical Review Letters **93**, 1–4 (2004).

[12]J. R. Brown and P. T. Callaghan, "Changing micellar order, lever rule behavior and spatio-temporal dynamics in shear-banding at the onset of the stress plateau," Soft Matter **7**, 10472–10482 (2011).
[13]C. J. Davies, A. J. Sederman, C. J. Pipe, G. H. McKinley, L. F. Gladden, and M. L. Johns, "Rapid measurement of transient velocity evolution using GERVAIS," Journal of Magnetic Resonance **202**, 93–101 (2010).
[14]Y. T. Hu and A. Lips, "Kinetics and mechanism of shear banding in an entangled micellar solution," Journal of Rheology **49**, 1001–1027 (2005).
[15]M. P. Lettinga and S. Manneville, "Competition between Shear Banding and Wall Slip in Wormlike Micelles," Physical Review Letters **103**, 1–4 (2009).
[16]E. Miller and J. P. Rothstein, "Transient evolution of shear-banding wormlike micellar solutions," Journal of Non-Newtonian Fluid Mechanics **143**, 22–37 (2007).
[17]H. Mohammadigoushki, A. Dalili, L. Zhou, and P. Cook, "Transient evolution of flow profiles in a shear banding wormlike micellar solution: experimental results and a comparison with the VCM model," Soft Matter **15**, 5483–5494 (2019).
[18]M. A. Fardin, T. Divoux, M. A. Guedeau-Boudeville, I. Buchet-Maulien, J. Browaeys, G. H. McKinley, S. Manneville, and S. Lerouge, "Shear-banding in surfactant wormlike micelles: Elastic instabilities and wall slip," Soft Matter **8**, 2535–2553 (2012).
[19]K. W. Feindel and P. T. Callaghan, "Anomalous shear banding: Multidimensional dynamics under fluctuating slip conditions," Rheologica Acta **49**, 1003–1013 (2010).
[20]S. Kuczera, C. Perge, M. A. Fardin, T. I. Brox, M. A. Williams, S. Manneville, and P. Galvosas, "Anomalous shear banding revisited with Rheo-NMR and Rheo-USV," Rheologica Acta **54**, 619–636 (2015).
[21]M. R. López-González, W. M. Holmes, P. T. Callaghan, and P. J. Photinos, "Shear banding fluctuations and nematic order in wormlike micelles," Physical Review Letters **93**, 1–4 (2004).
[22]M. A. Fardin, O. Cardoso, B. Lasne, G. Grégoire, J. P. Decruppe, M. Argentina, and S. Lerouge, "Taylor-like vortices in the shear-banding flow of giant micelles," AIP Conference Proceedings **1027**, 192–194 (2008), arXiv:0909.0766.
[23]M. A. Fardin, T. J. Ober, V. Grenard, T. Divoux, S. Manneville, G. H. McKinley, and S. Lerouge, "Interplay between elastic instabilities and shear-banding: Three categories of Taylor-Couette flows and beyond," Soft Matter **8**, 10072–10089 (2012).
[24]M. E. Helgeson, P. A. Vasquez, E. W. Kaler, and N. J. Wagner, "Rheology and spatially resolved structure of cetyltrimethylammonium bromide wormlike micelles through the shear banding transition," Journal of Rheology **53**, 727–756 (2009).
[25]A. K. Gurnon, C. López-Barrón, M. J. Wasbrough, L. Porcar, and N. J. Wagner, "Spatially resolved concentration and segmental flow alignment in a shear-banding solution of polymer-like micelles," ACS Macro Letters **3**, 276–280 (2014).
[26]P. Rassolov and H. Mohammadigoushki, "Effects of elasticity and flow ramp up on kinetics of shear banding flow formation in wormlike micellar fluids," Journal of Rheology **64**, 1161–1177 (2020).
[27]S. Lerouge, M. A. Fardin, M. Argentina, G. Gregoire, and O. Cardoso, "Interface dynamics in shear-banding flow of giant micelles," Soft Matter **4**, 1808–1819 (2008), arXiv:arXiv:0804.0374v1.
[28]M.-A. Fardin, L. Casanellas, B. Saint-Michel, S. Manneville, and S. Lerouge, "Shear-banding in wormlike micelles: Beware of elastic instabilities," Journal of Rheology **60**, 917–926 (2016).

[29]S. Lerouge, M. Argentina, and J. P. Decruppe, "Interface instability in shear-banding flow," Physical Review Letters **96**, 1–4 (2006).
[30]H. Mohammadigoushki and S. J. Muller, "A flow visualization and superposition rheology study of shear-banding wormlike micelle solutions," Soft Matter **12**, 1051–1061 (2016).
[31]L. Zhou, L. P. Cook, and G. H. McKinley, "Multiple Shear-Banding Transitions for a Model of Wormlike Micellar Solutions," SIAM Journal on Applied Mathematics **72**, 1192–1212 (2012).
[32]L. Zhou, G. H. McKinley, and L. P. Cook, "Wormlike micellar solutions: III. VCM model predictions in steady and transient shearing flows," Journal of Non-Newtonian Fluid Mechanics **211**, 70–83 (2014).
[33]J. M. Adams, S. M. Fielding, and P. D. Olmsted, "Transient shear banding in entangled polymers: a study using the Rolie-Poly model," Journal of Rheology **55**, 1007–1032 (2011), arXiv:1011.4355.
[34]D. B. Allan, T. Caswell, N. C. Keim, and C. M. van der Wel, "soft-matter/trackpy: Trackpy v0.4.2," (2019).
[35]H. Mohammadigoushki and S. J. Muller, "Inertio-elastic instability in Taylor-Couette flow of a model wormlike micellar system," Journal of Rheology **61**, 683–696 (2017).
[36]C. J. Dimitriou, L. Casanellas, T. J. Ober, and G. H. McKinley, "Rheo-PIV of a shear-banding wormlike micellar solution under large amplitude oscillatory shear," Rheologica Acta **51**, 395–411 (2012).
[37]R. Granek and M. E. Cates, "Stress relaxation in living polymers: Results from a Poisson renewal model," The Journal of Chemical Physics **96**, 4758–4767 (1992).
[38]R. Granek, "Dip in $G''(\omega)$ of Polymer Melts and Semidilute Solutions," Langmuir **10**, 1627–1629 (1994), https://doi.org/10.1021/la00017a051.
[39]G. Tan, W. Zou, M. Weaver, and R. G. Larson, "Determining threadlike micelle lengths from rheometry," Journal of Rheology **65**, 59–71 (2021).
[40]W. Zou, G. Tan, H. Jiang, K. K. Vogtt, M. Weaver, P. Koenig, G. Beaucage, and R. G. Larson, "From well-entangled to partially-entangled wormlike micelles," Soft Matter **15**, 642–655 (2019).
[41]C. Oelschlaeger, M. Schopferer, F. Scheffold, and N. Willenbacher, "Linear-to-branched micelles transition: A rheometry and diffusing wave spectroscopy(DWS) study," Langmuir **25**, 716–723 (2009).
[42]P. A. Vasquez, G. H. McKinley, and L. Pamela Cook, "A network scission model for wormlike micellar solutions," Journal of Non-Newtonian Fluid Mechanics **144**, 122–139 (2007).